Journal of Sol-Gel Science and Technology
https://doi.org/10.1007/s10971-023-06049-2

ORIGINAL PAPER: SOL-GEL AND HYBRID MATERIALS FOR ENERGY, ENVIRONMENT AND BUILDING APPLICATIONS

Application of CuO and its composite with polyaniline on the photocatalytic degradation of methylene blue and the Cr(VI) photoreduction under visible light

Ozcan Koysuren[1] · Hafize Nagehan Koysuren[2]

Received: 15 October 2022 / Accepted: 17 January 2023

Abstract

Copper oxide (CuO) as the photocatalyst nanoparticle was prepared by the solution combustion technique. During the synthesis, iron atom source, which was iron nitrate, was added to the reaction medium to obtain iron doped CuO nanoparticles. In addition, the iron doped CuO nanoparticles were combined with the conducting polymer, which was polyaniline, through the in-situ polymerization technique. The chemical and crystal structure, optical property and the photocatalytic activity of the CuO nanoparticles and their composites were studied as a function the dopant atom concentration of CuO and the photocatalyst composition of the composites. The prepared samples were characterized by Fourier-transform infrared spectroscopy, X-ray powder diffraction, X-ray photoelectron spectroscopy, fluorescence spectroscopy, field emission scanning electron microscopy, energy dispersive X-ray (EDX) spectroscopy and UV-Vis absorption spectroscopy. The photocatalytic activity of the prepared samples was evaluated by the photocatalytic degradation of a model dye, methylene blue, under visible light irradiation. In addition, the Cr(VI) photoreduction efficiency of the prepared samples were studied. Iron atoms might enter into the substitutional sites of CuO. The iron atoms might act as a trapping center to capture the photoinduced charge carriers of CuO, promoting both the charge separation and the photocatalytic activities. The photocatalytic dye degradation efficiency and the Cr(VI) photoreduction efficiency of the iron doped CuO increased by almost 17% compared to undoped CuO. The composites with low polyaniline content might promote the charge separation because of the difference between the band potentials of CuO and polyaniline as shown in the graphical abstract. The composite with 80 wt.% of the iron doped CuO exhibited the highest photocatalytic dye degradation of almost 72% and the Cr(VI) photoreduction efficiency of almost 56%.

Supplementary information The online version contains supplementary material available at https://doi.org/10.1007/s10971-023-06049-2.

✉ Ozcan Koysuren
koysuren@ankara.edu.tr

[1] Department of Energy Systems Engineering, Ankara University, Ankara 06830, Turkey

[2] Department of Environmental Engineering, Kirsehir Ahi Evran University, Kirsehir 40100, Turkey

Published online: 06 February 2023

Graphical abstract

Proposed photocatalytic dye degradation and Cr(VI) photoreduction mechanism of CuO-Fe3/Pani

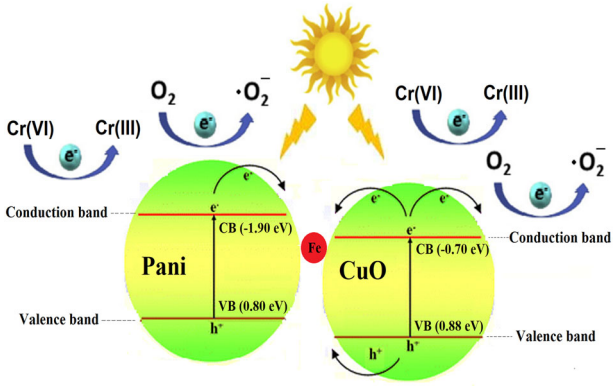

Keywords CuO · Polyaniline · Doping · Photocatalytic dye degradation · Cr(VI) photoreduction

Highlights

- Doping CuO with iron atom and coupling CuO with polyaniline enlarged the optical band gap energy and enhanced both the photocatalytic dye degradation efficiency and the Cr(VI) removal efficiency.
- Doped CuO and CuO/Polyaniline composites provided low recombination rate of the photogenerated charge carriers.
- Superoxide radicals dominated the photocatalytic dye degradation reaction.
- The potential for use of CuO as a photocatalyst has been increased by doping with iron atom and compounding with polyaniline.

1 Introduction

Environmental pollution has become one of the most concerned issues in the sustainable development of human society all over the world. The treatment of organic pollutants in the wastewater has attracted great attention among the scientists, studying mainly on the environmental issues. Especially, the organic dyes, released to the aquatic environment by the textile, paper, leather, coating and photochemical industries, are not self-degradable and lead to severe environmental contamination both in aquatic system and terrestrial system [1]. The organic dye molecules can affect the biological cycles, especially the photosynthesis process. Organic dye molecules can absorb a broad spectrum of visible light, giving rise to a reduction in the amount of light used for the photosynthesis. In addition, some of the organic dyes are known to be as carcinogenic. Thus, it is important to separate the organic dyes from the wastewater prior to the discharge into rivers or oceans [2]. In addition to organic dyes, hexavalent chromium (Cr(VI)) is a highly toxic metal ion, leading to serious health problems such as cancer and liver damage. Cr(VI) ions are also commonly found in the wastewater of certain industries such as mining, metal plating and leather. The Cr(VI) pollution in the wastewater has become a serious environmental problem. It is also important to eliminate the Cr(VI) ions in wastewater before they are released into the environment [3].

Photocatalytic decolorization based on the use of a semiconducting photocatalyst is an effective technique for the treatment of the wastewater [4, 5]. In addition, the photoreduction of highly toxic Cr(VI) ions to less toxic Cr(III) ions using the semiconducting photocatalyst has been considered to be an environmentally promising technology [3]. CuO, a p-type semiconductor, has a narrow band gap and has been utilized in various applications such as gas sensors, lithium-ion electrode materials, supercapacitor electrode materials, optical switch and heterogeneous catalysis [4, 5]. In recent years, intensive studies have been carried out on the photocatalytic dye degradation application of CuO because of its superior properties such as redox selectivity, chemical and physical stability, and low production cost. The main drawback of CuO is the high recombination rate of the photoexcited charge carriers under illumination [6]. In order to improve the photocatalytic activity of CuO, metal or non-metal doping has been applied to CuO. The optical and electronic properties of CuO, especially the photocatalytic activity, vary depending on its morphological and crystal structure. The morphology and especially the crystal structure determine the energy band diagram of the semiconducting material. It has been known that metal or non-metal doping could lead to a

change in the crystal structure and the reactivity of the semiconducting material, which could also affect both the energy band diagram and the photocatalytic activity. In addition, the metal or non-metal doping could result in the formation of structural defect such interstitial defects and oxygen vacancies, which might enhance the intensity of the charge carriers and suppress the recombination rate of the photoexcited electron-hole pairs [7]. In the literature, CuO was doped with nickel atom [8], cerium atom [7], zinc atom [9], lanthanum atom [6], silver atom [10], lithium atom [11], cadmium atom [12], manganese atom [13], erbium atom [14], molybdenum atom [15], magnesium atom [16] and iron atom [5, 17, 18], respectively. George et al. (2022) obtained an optical band gap of 2.26 eV with the iron doped CuO. The photocatalytic dye degradation efficiency of the iron doped CuO was found to be 62% under the visible light illumination (500 W Xenon lamp) at 60 min [18]. As an example of non-metal doping, CuO was doped with nitrogen atom [19] and carbon atom [20], respectively. Doping CuO with a metal or non-metal atom to enhance the Cr(VI) photoreduction efficiency is also a promising strategy. In the literature, CuO/Cu_2O composite was doped with Ag atom [21] and TiO_2/CuO composite was doped with Cu atom [22] to enhance the Cr(VI) photoreduction efficiency of the CuO based composites.

As an alternative to the metal or non-metal doping, coupling the semiconducting material with a conducting polymer could yield composites with enhanced photocatalytic activity. Polyaniline as a conducting polymer has been known as a good photosensitizer and contributes to the photocatalytic activity of the semiconducting materials with its specified features. Polyaniline is a highly conducting polymer, possessing π conjugated electrons on the backbone of its polymer chain and can absorb the visible light spectrum of the sunlight. Under a light source, the valence band electrons of polyaniline can be excited to its conduction band to form photoexcited electron-hole pairs. The specified properties of polyaniline allow it to be involved in the photocatalytic dye degradation process [23]. In the literature, within the scope of the study of the photocatalytic degradation of organic pollutants, polyaniline was compounded with TiO_2 [24], $SrSnO_3$ [25], ZnO [26], WO_3 [27], AgCl [28] and BiOCl [29], respectively. Faisal et al. [25] prepared the composite of $SrSnO_3$ with polyaniline, which resulted in the formation of a heterojunction structure between the composite components, accompanied by an increase in the degradation of organic pollutants in water due to the promotion of the photoexcited charge carriers. The photocatalytic degradation efficiency of methylene blue for the polyaniline/$SrSnO_3$ (5/95 wt./wt.) composite was 83% at 240 min [25].

Within the scope of this study, CuO was doped with iron (Fe) atoms. It was thought that the iron atom might act as an electron trap as shown in the graphical abstract, improving both the photocatalytic dye degradation efficiency and the Cr(VI) photoreduction efficiency of CuO. Although there are a few studies on the photocatalytic dye degradation efficiency of the iron doped CuO in the literature, no studies were found on the Cr(VI) photoreduction efficiency of the iron doped CuO and its composite with polyaniline. Unlike the studies in the literature, in this study, the iron doped CuO was also coupled with polyaniline. In addition to the dye degradation activity, the Cr(VI) removal efficiency of the prepared samples was studied. Because of the difference between the band potentials of CuO and polyaniline, coupling CuO nanoparticles with polyaniline in the composite structure might promote the charge separation on CuO, enhancing the photocatalytic activity.

2 Experimental

2.1 Materials and methods

CuO nanoparticles were synthesized through the solution combustion technique. For this purpose, copper(II) nitrate trihydrate ($CuO(NO_3)_2{\cdot}3H_2O$), which was the oxidizer, and citric acid ($C_6H_8O_7{\cdot}H_2O$), which was the fuel, were to used to synthesize CuO in nanoparticle morphology. CuO was thought to be synthesized according to the reaction given below [30]:

$$CuO(NO_3)_2{\cdot}3H_2O + C_6H_8O_7 \cdot H_2O \rightarrow CuO + \text{gaseous products} \quad (1)$$

The oxidizer and the fuel were used in a 1/1 (mol/mol) stoichiometric ratio. The specified chemicals, copper(II) nitrate trihydrate (1.0 g) and citric acid (0.869 g), were dissolved in distilled water (30 ml) using a magnetic stirrer. The solution was then continued to be stirred on a preheated plate at 100 °C. The solution started to evaporate in a few hours and turned into a viscous gel. When the heating continued at 100 °C, the viscous gel began to a self-sustaining combustion reaction. The as-prepared material was ground to fine powder and calcinated at 400 °C for 4 h to obtain CuO nanoparticles in the crystal structure. To obtain the iron doped CuO, iron (III) nitrate nonahydrate ($Fe(NO_3)_3{\bullet}9H_2O$) as the iron (Fe) atom source was added into the copper(II) nitrate trihydrate-citric acid solution before heating. The weight ratio of both Fe to CuO were adjusted to be 1, 3 and 5%, respectively. The same process steps applied to produce undoped CuO were followed to produce the iron doped CuO. The samples doped with 1, 3 and 5 wt.% Fe atoms were named as CuO-Fe1, CuO-Fe3 and CuO-Fe5, respectively.

The in-situ polymerization technique was applied to couple the iron doped CuO nanoparticles with polyaniline (Pani) in the composite structure. Pani was obtained through the oxidation of aniline hydrochloride ($C_6H_5NH_2{\cdot}HCl$), monomer, with ammonium peroxydisulfate ($(NH_4)_2S_2O_8$), oxidant, according to the reaction (2). The molar ratio of the monomer to the oxidant was set to 4/5 [31].

$$4nC_6H_5NH_2 \cdot HCl + 5n(NH_4)_2S_2O_8 \rightarrow 4\left([C_6H_4NH]_2[C_6H_4NH^+Cl^-]_2\right)n + 2nHCl + 5nH_2SO_4 + 5n(NH_4)_2SO_4 \quad (2)$$

In detail, aniline hydrochloride was dissolved in distilled water to obtain a 0.04 M solution. CuO nanoparticles were dispersed in the monomer solution and stirred for 1 h. using the magnetic stirrer. At the same time, ammonium peroxydisulfate was dissolved in distilled water in a separate beaker to obtain a 0.05 M solution. Then, the oxidant solution was added into the monomer solution. The as-prepared solution was stirred overnight. Next day, the composite precipitate was collected on filter and rinsed with acetone. Finally, the composite particles were dried at 60 °C for 24 h [32]. The CuO ratio of the composite structure was set to 20, 40, 60, 80 wt.%, respectively. For this purpose, CuO-Fe3 nanoparticles, which provided the highest photocatalytic activity among the iron doped CuO, were used. In order to distinguish among the composite samples, they were labeled as CuO-Fe3/Pani(x/100-x) (x = 20, 40, 60, 80), respectively.

3 Structural, morphological and optical characterization

Fourier-transform infrared (FTIR) spectroscopy of the prepared samples was acquired from 400 cm^{-1} to 4000 cm^{-1} by Perkin Elmer 400 model spectrophotometer with a resolution of 4 cm^{-1}. FTIR spectra was used to reveal the chemical structure of both undoped and doped CuO, and their composites with polyaniline. The X-ray diffraction (XRD) pattern of the prepared samples was obtained with Inel Equinox 1000 model X-ray diffractometer using a CoKα radiation source (λ = 1.788970 Å) at 30 mA and 30 kV with scanning in the range of 20° to 70°. The crystal structure of both undoped and doped CuO and their composites with polyaniline was studied. X-ray photoelectron spectroscopy (XPS) analysis of CuO and the iron doped CuO was conducted on a PHI 5000 VersaProbe model XPS instrument operating with a monochromated Al Kα radiation source (1486.6 eV). The structural effect of the iron doping on CuO was investigated using the XPS spectra. The fluorescence spectroscopy was utilized to compare the recombination rate of the photoexcited charge carriers on the photocatalyst samples. The fluorescence spectrum of the CuO nanoparticles and the composite samples was recorded on a Lumina model fluorescence spectrophotometer (Thermo Scientific) at the excitation wavelength of 320 nm. The morphology of the samples was studied using a field emission scanning electron microscope (FE-SEM, QUANTA 400 F). The elemental composition of the samples was investigated by energy dispersive X-ray (EDX) spectroscopy (JXA-8230 EDX Microanalysis Instrument). The UV–Vis absorption spectroscopy of all samples was acquired from 200 nm to 800 nm using a UV–Vis spectrophotometer (Genesys 10 S, Thermo Scientific).

4 Characterization of the photocatalytic performance

The photocatalytic dye degradation activity of the as-prepared samples was investigated using methylene blue as a model dye in an aqueous solution under visible light irradiation. To prepare the model dye solution, methylene blue (1.0 mg) was dissolved in distilled water (100 ml) and then the as-prepared photocatalyst sample (50 mg) was dispersed in the methylene blue solution in the dark for half an hour to ensure equilibrium of the prepared solution. Afterward, the suspension was exposed to visible light irradiation using a 300 W lamp (Osram Ultravitalux) under stirring. A distance of about 15 cm between the visible light lamp and the suspension was maintained. To keep the temperature of the suspension constant, the system was ventilated by a fan. After the visible light irradiation, a sample (3 ml) was taken from the suspension. The sample suspension was centrifuged to remove the photocatalyst particles from the dye solution. The photocatalytic dye degradation efficiency was monitored using the UV–Vis spectrophotometer every 30 min. The percentage of the photocatalytic degradation of methylene blue was calculated using the following Eq. (3):

$$Dye\ degradation\ eff.\% = (C_0 - C)/C_0 \times 100 \quad (3)$$

where C_0 and C are the solution concentrations before the visible light illumination and after the visible light illumination, respectively [33].

The following pseudo-first-order kinetic model (4) was utilized to evaluate the reaction kinetics of the methylene blue degradation [34]:

$$ln(C_0/C) = kt \quad (4)$$

The reaction rate constant k can be obtained from the slope of the $ln(C_0/C)$ vs. t graph from 0 to 240 min.

To study the effect of reactive radicals formed during the photocatalytic dye degradation reaction, tert-butanol (6 ml/

100 ml dye solution) as a hydroxyl radical scavenger and ascorbic acid (1 mg/100 ml of the dye solution) as a superoxide radical scavenger were dispersed in the model dye solution in the presence CuO and CuO-Fe3, respectively [35]. In order to evaluate the effects of ambient conditions on the photocatalytic degradation of the model dye, hydrogen peroxide (H_2O_2) (1 ml/100 ml dye solution) was added into the dye solution, containing CuO, CuO-Fe3 and CuO-Fe3/Pani(80/20), respectively. In addition, the ambient pH of the model dye solutions, containing undoped CuO, CuO-Fe3 and CuO-Fe3/Pani(80/20), separately, was adjusted to 4 and 10 using HCl (0.1 M) and NaOH (0.1 M), respectively. In addition to the simulated organic dye solutions, it was planned to evaluate the efficiency of the photocatalyst samples, CuO, CuO-Fe3 and CuO-Fe3/Pani(80/20), in real wastewater sample obtained from Ankara Central Wastewater Treatment Plant. The real wastewater experiment was similar to that of the simulated dye solution experiment except the utilization of wastewater instead of distilled water. Within the scope of the reusability test, the dye solution was centrifuged at 7000 rpm to separate the photocatalyst samples. Then, they were rinsed with distilled water and dried at 60 °C. The dried photocatalyst particles were re-dispersed in the dye solution for the next cycle of the photocatalytic dye degradation experiment [36]. To evaluate the effect of the initial solution concentration on the photocatalytic dye degradation efficiency, the simulated dye solution with different initial solutions concentrations of methylene blue (10, 20, 30 and 40 mg/l) was prepared. In addition, the photocatalyst (CuO-Fe3/Pani(80/20)) concentration of the simulated dye solution was changed in the range of 0.25 g/l–1.0 g/l to study the effect of photocatalyst concentration on the photocatalytic dye removal rate.

The Cr(VI) photoreduction experiment of the prepared samples was also conducted under the visible light irradiation. To prepare a simulated Cr(VI) solution, 2 mg of $K_2Cr_2O_7$ was disperse in 100 ml of distilled water. 50 mg of the prepared samples was added into the as-prepared solution. After the adsorption-desorption equilibrium attained between the photocatalyst particles and the Cr(VI) ions, the Cr(VI) solution was exposed to the visible light irradiation. A sample (2 ml) was extracted from the Cr(VI) solution every 60 min and was centrifuged to separate the photocatalyst particles from the sample solution. The Cr(VI) concentration of the supernatant solution was measured by diphenylcarbazide photometric technique [37]. The percent photoreduction of Cr(VI) was calculated using the following equation [22]:

$$\%\, Cr(VI)\, photoreduction = (C_0 - C^*)/C_0 \times 100 \qquad (5)$$

where C_0 is the initial concentration of the Cr(VI) solution and C^* is the concentration of the Cr(VI) solution at the time the sample is taken.

5 Results and discussion

5.1 FTIR analysis

Chemical structure of the as-prepared samples was investigated using FTIR spectroscopy. Figure 1 exhibits FTIR spectrum of CuO, CuO-Fe3 and CuO-Fe3/Pani(80/20). The transmission peaks observed at around 475 and 593 cm^{-1} were attributed to the stretching vibration of the Cu-O bond (Fig. 1a) [38]. When compared with the FTIR spectrum of CuO, the spectrum of the CuO-Fe3 (Fig. 1b) does not exhibit distinct shift in the wave number. The intensity of the transmission peak observed at around 593 cm^{-1} seems to decrease slightly with the iron doping. It is clear that CuO was synthesized successfully. There are two additional transmission peaks at around 1365 and 1738 cm^{-1} on the FTIR spectrum of CuO and CuO-Fe3, which might be linked to bending vibrations of the asymmetric C-O structure and the O-H bond, respectively [39, 40]. The noticed transmission peaks do not belong to the CuO chemical structure. The reason for these transmission peaks might be the precursor chemicals used to synthesize CuO. On the other hand, the iron doping does not seem to change the chemical bond structure of CuO.

Figure 1c exhibits FTIR spectrum of CuO-Fe3/Pani(80/20). The composite sample exhibits the transmisson peak at around 800 cm^{-1}, which was assigned to the out of plane vibrations of the =C-H bond of polyaniline [41]. The transmission peak at around 1150 cm^{-1} might belong to the plane bending vibration of the C-H bond on the aromatic structure. The peak seen at around 1300 cm^{-1} was due to characteristic vibrations of the protonated polyaniline. The indicated peak can be thought as a measure of the degree of delocalization of Pani electrons [42]. The peaks present at around 1050 and 1230 cm^{-1} were attributed to the C-N stretching vibration of the benzenoid structure and the peak present at around 1490 cm^{-1} was attributed to the C = C

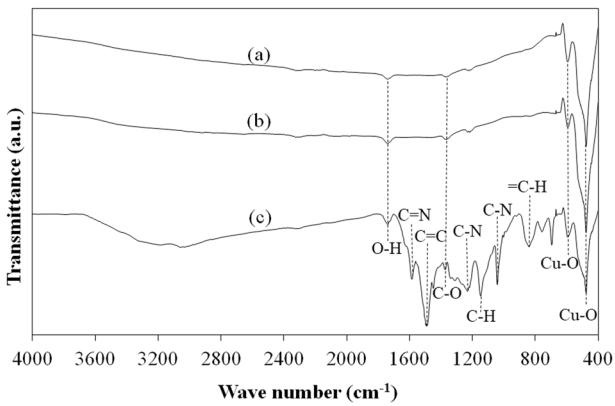

Fig. 1 FTIR spectroscopy analysis: FTIR spectrum of **a** CuO, **b** CuO–Fe3 and **c** CuO–Fe3/Pani(80/20)

stretching vibration of the benzenoid structure. The transmission peak at around 1590 cm^{-1} might be due to the C = N stretching vibration of the quinonoid structure of the conducting polymer. The transmisson band observed between 3200–3600 cm^{-1} was assigned to the stretching vibration of the N-H bond [41]. The composite sample also exhibit the characteristic transmisson peaks of CuO at around 475 and 593 cm^{-1} (Fig. 1c) [38].

5.2 XRD analysis

XRD diffractogram of undoped CuO exhibits the typical diffraction peaks of the CuO crystal structure, which were attributed to the monoclinic CuO crystal structure (JCPDS No. 05-0661) [6]. On the XRD diffractogram of CuO (Fig. 2a), there are diffraction peaks at 37.20°, 40.62°, 44.28°, 50.59°, 56.23°, 61.72°, 67.45°, 71.68°, 75.07°, 77.38° and 79.54°, which might be indexed to (−111), (200), (−112), (−202), (202), (−113), (−311), (220), (312), (311) and (−204) planes of the monoclinic CuO crystal. The diffraction peak intensities and their widths indicated the crystalline nature of the synthesized CuO nanoparticles (Fig. 2) [43]. With the iron doping, the intensity of the diffraction peaks of CuO at 40.62°, 44.28°, 75.07° and 79.54° decreased slightly. In addition, the diffraction peaks of CuO at 67.45°, 75.07° and 79.54° shifted toward higher diffraction angles, revealing that the iron atoms were successfully integrated into the CuO crystal structure (Fig. 2b) [7]. The slight decrease in the specified peak densities indicated that the iron atoms slightly disrupted the crystal structure of CuO. The average crystallite size, calculated using the Scherrer formula, decreased from 15.08 to 13.69 nm with the iron doping [43]. According to the XRD diffractogram of CuO and CuO-Fe3 (Figs. 2a and 2b), all the diffraction peaks belong to the CuO crystal structure and no different peaks were observed, revealing that the iron doping did not result to form any new phase in the CuO crystal structure. The XRD diffractogram of CuO-Fe3/Pani(80/20) is illustrated in Fig. 2c. Figure 2c exhibits a broad band with a low intensity at around 25°, which might be due the amorphous polymer phase of the composites [44, 45]. On the diffractogram of the CuO-Fe3/Pani(80/20) composite (Fig. 2c), the peaks at 37.50°, 40.95°, 44.64°, 50.70°, 56.56°, 62.17°, 67.91°, 72.06° and 77.46° belong to the characteristic crystal planes of CuO. When compared with undoped CuO and CuO-Fe3, the diffraction peaks of CuO shifted toward higher diffraction angles, which might be due to the interaction between the conducting polymer and CuO-Fe3.

In the context of the reusability test of the as-prepared catalysts, the stability of CuO nanoparticles after the photocatalytic degradation study was studied using the XRD analysis. Figure 2d shows the XRD diffractogram of the four times of recycled CuO. For the four times of recycled CuO, the characteristic diffraction peaks of CuO shifted slightly toward lower diffraction angles and the intensity of the characteristic diffraction peaks decreased slightly (Fig. 2d). No additional diffraction peaks were observed on the XRD diffractogram of the four times of recycled CuO, revealing no structural changes on CuO. According to the XRD analysis, CuO retained its crystalline structure to some extent and is a suitable photocatalyst for repeated uses.

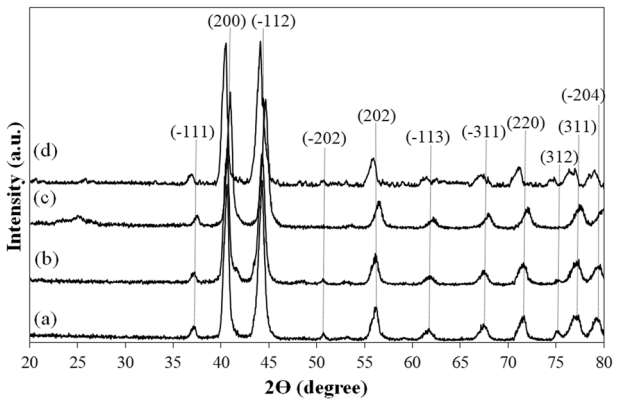

Fig. 2 XRD spectroscopy analysis: XRD spectrum of **a** CuO, **b** CuO–Fe3, **c** CuO–Fe3/Pani(80/20) and **d** four times of recycled CuO

5.3 XPS analysis

XPS analysis was performed to investigate the chemical content of both undoped and doped CuO and the electronic state of elements within the CuO structure. The overall spectrum of the iron doped CuO is illustrated in Fig. 3a, which reveals the presence of the dopant atoms in CuO in addition to Cu and O atoms. Besides the peaks linked to the Cu, O and Fe atoms, there is a peak in the overall spectrum of all samples at ~280 eV belonging to the C atom, which might result from the precursor chemicals of CuO (Fig. 3a). The Cu 2p spectra of CuO illustrates the Cu 2p3/2 peak at 931.5 eV with two satellite peaks at 939.8 and 942.8 eV, respectively (Fig. 3b). Also, the Cu 2p spectra exhibits the Cu 2p1/2 peaks a 951.7 eV with a satellite peak at 961.3 eV. The noticed peaks can be attributed to the Cu^{2+} state of copper atoms within the CuO structure [46]. There was a small shift toward lower energy in the binding energy of the peaks with the iron doping (Fig. 3b). There was an increase and a decrease in the peak intensity at 931.5 eV with CuO-Fe1 and CuO-Fe3, respectively.

The O 1 s spectra of CuO exhibits two peaks at 528.4 and 530.3 eV, which were assigned to the O^{2-} state of oxygen within the CuO structure and surface adsorbed O_2 molecules, respectively (Fig. 3c) [46]. Compared to CuO, the peaks of the O 1 s spectrum for both CuO-Fe1 and CuO-Fe3 shifted slightly towards lower binding energy and increased

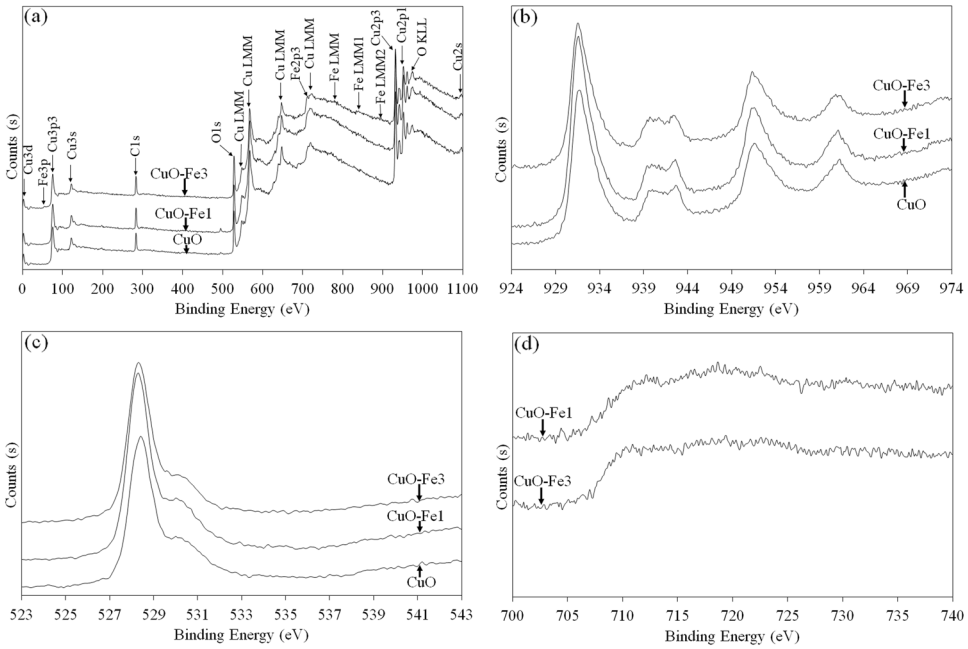

Fig. 3 XPS spectroscopy analysis: **a** XPS general survey spectrum and high resolution XPS spectrum of **b** Cu 2p, **c** O 1s, **d** Fe 2p obtained for the iron doped CuO

significantly in intensity (Fig. 3c). The Cu 2p spectra and the O 1 s spectra indicated that both undoped and doped CuO was synthesized successfully. The Fe 2p spectrum of CuO-Fe1 and CuO-Fe3 exhibits two broad peaks at approximately 710 and 720 eV (Fig. 3d), which were attributed to the Fe 2p3/2 and Fe 2p1/2 electronic states of the Fe atom, respectively. The noticed peaks revealed that the iron atom was integrated into the chemical structure of CuO [47].

5.4 Fluorescence study

To reveal the effect of doping of CuO with the iron atom, and the effect of compounding CuO with polyaniline, the fluorescence spectrum of the CuO, CuO-Fe3 and CuO-Fe3/Pani(80/20) samples was compared on Fig. 4. The main reason for the fluorescence emissions was the recombination of the photoexcited electron-hole pairs. In addition, the intensity of the emission bands is directly proportional to the recombination rate of the photoexcited charge carriers. In general, the lower fluorescence band intensity indicated the suppressed recombination rate, which results in an enhanced photocatalytic activity [48]. According to Fig. 4, all samples exhibited two emission bands in the range of 470–520 nm and 660–620 nm, respectively. The emission band observed between 470–520 nm might be due to the oxygen vacancy. The singly ionized oxygen vacancy could emit the specified emission as a result of the recombination of a singly ionized electron with a photoinduced hole. Another major emission band might be attributed to the interstitial defect of the interstitial copper atoms or anti-oxygen sites [49]. High emission intensity of undoped CuO implied that the recombination rate

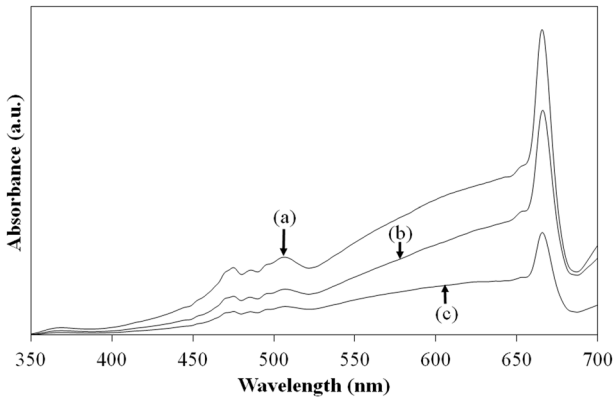

Fig. 4 Fluorescence spectroscopy analysis: Fluorescence spectrum of **a** CuO, **b** CuO–Fe3 and **c** CuO–Fe3/Pani(80/20)

of the photoinduced charge carriers on CuO was high. The emission intensity of both bands of CuO-Fe3 was lower than that of undoped CuO (Fig. 4b), which revealed that the recombination rate of the photoexcited electron-hole pairs of CuO was suppressed with the iron atom doping. In addition, the emission intensity of both bands of the composite sample was lower than that of CuO, implying that compounding CuO-Fe3 with polyaniline suppressed the recombination rate of the photogenerated charge carriers on CuO-Fe3. Among the samples, the CuO-Fe3/Pani(80/20) composite exhibited the lowest emission intensities (Fig. 4c).

5.5 Morphological analysis

Figures 5 and 6 exhibit the FESEM images and EDX spectrum of CuO, CuO-Fe1, CuO-Fe3, CuO-Fe3/Pani(40/60)

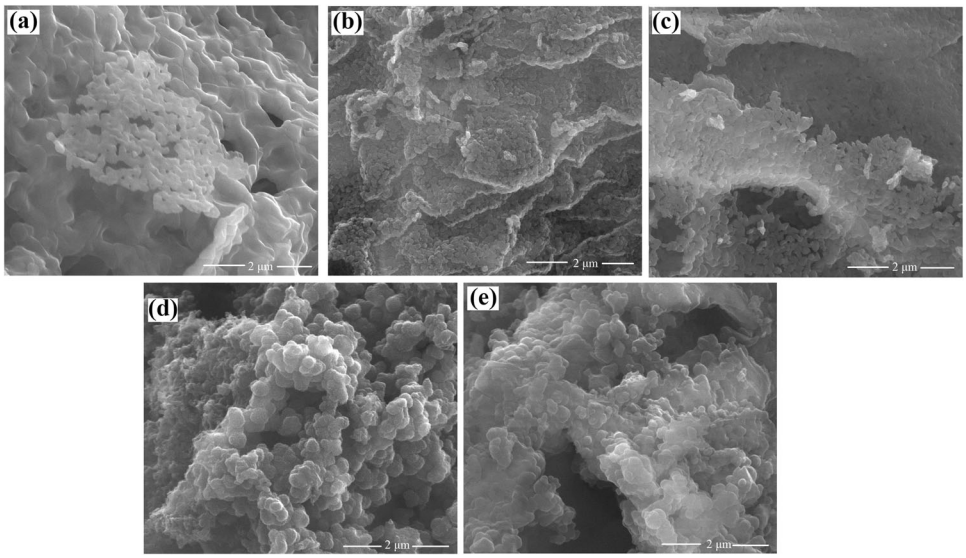

Fig. 5 Morphology analysis: SEM images of **a** CuO, **b** CuO–Fe1, **c** CuO–Fe3, **d** CuO–Fe3/Pani(40/60) and **e** CuO-Fe3/Pani(80/20)

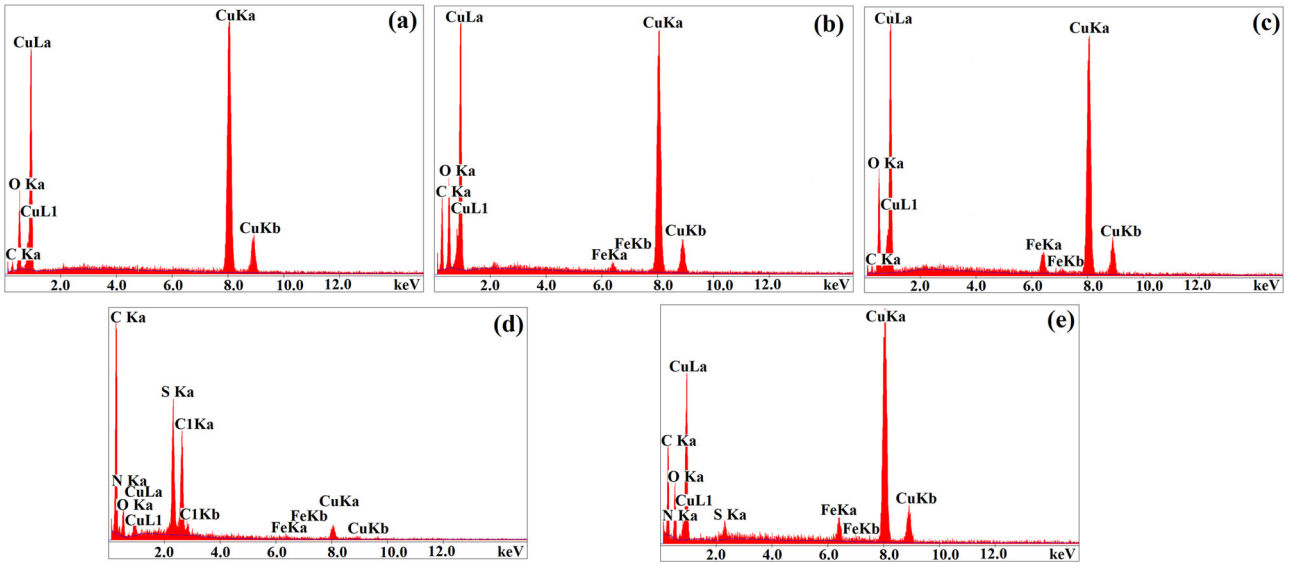

Fig. 6 EDX spectroscopy analysis: EDX spectrum of **a** CuO, **b** CuO–Fe1, **c** CuO–Fe3, **d** CuO–Fe3/Pani(40/60) and **e** CuO–Fe3/Pani(80/20)

and CuO-Fe3/Pani(80/20). These images displayed the uniform morphology of round-like nanoparticles belonging to both doped and undoped CuO. The size of undoped CuO nanoparticles were about 100–200 nm in diameter (Fig. 5a). No significant change in particle size and shape was observed with the iron doping (Figs. 5b and 5c). The elemental composition of the specified nanoparticles was obtained by using the EDX spectroscopy. According to the EDX analysis (Fig. 6a), CuO was composed of Cu, O and C atoms. The presence of the C peak on the EDX spectrum of CuO indicated that the CuO precursor chemicals might not be converted to CuO completely. The EDX spectrum of the iron doped CuO exhibits the peaks belonging to Cu, O, C, Fe atoms. The presence of the iron atom in CuO was proved. The EDX spectrum of the iron doped CuO also exhibits the C peak (Fig. 6b-c).

Figures 5d, e and 6d, e illustrate the FESEM images and the EDX spectrum of CuO-Fe3/Pani(40/60) and CuO-Fe3/Pani(80/20). These images exhibit that the iron doped CuO nanoparticles were covered with a thin polyaniline layer. When the CuO-Fe3/Pani(40/60) composite and the CuO-Fe3/Pani(80/20) composite were compared, the thickness of the polymer layer coated on the CuO-Fe3 nanoparticles seemed to be almost the same (Fig. 5d, e). The EDX spectrum of the composite samples revealed the successful coating of Pani on to the photocatalyst nanoparticles. The EDX spectrum of the polyaniline composites depicts the peaks belonging to C, N, O, S and Cu atoms (Fig. 6d, e).

In order to investigate the stability of the CuO nanoparticles after the photocatalytic degradation study, the FESEM images of the four times of recycled CuO, CuO-Fe3 and CuO-Fe3/Pani(80/20) were also obtained (Fig. 7).

The FESEM images illustrate sphere-like structures of CuO in agglomated form. No significant changes in pure and doped CuO morphology was observed, which showed that CuO maintained its stability after the photocatalytic dye degradation tests.

5.6 UV-Visible absorption study

Figure 8a illustrate the UV-Vis absorption spectrum of undoped and doped CuO nanoparticles prepared with varying dopant amounts of Fe atoms. Both undoped and the iron doped CuO nanoparticles exhibited light absorption in the wavelength range of 200–250 and 250–750 nm (Fig. 8a). The absorption intensity of the iron doped CuO nanoparticles was higher than that of undoped CuO in the wavelength of 250–750 nm, indicating the enhancement of light absorption ability of CuO with the iron doping (Fig. 8a). The increase in the light absorption ability was parallel to the increase in the iron atom content. In the literature, Zhu et al. (2015) observed a red shift with the iron doping [5]. However, a blue shift was observed with the iron doping in the present study, which might be attributed to the interaction of the conduction band electrons with the 3d electrons of the iron atom [7].

UV-Visible absorption spectrum of the CuO-Fe3/Pani composites illustrates the absorption peaks at around 270 and 550 nm. The peak at 270 nm might be assigned to $\pi \rightarrow \pi*$ transition or exciton transition. The peak observed at 550 nm might be attributed to the polaron-$\pi*$ and π-polaron transition on the cationic species of polyaniline [50]. As the content of the conducting polymer in the composite increased, the intensity of the specified peaks at 270 and 550 nm increased. According to Fig. 8b, combining CuO-Fe3 with polyaniline within the composite structure seemed to be beneficial in terms of the visible light absorption ability of doped CuO. Polyaniline was a good sensitizer for CuO and expanded the photoactive region of undoped and doped CuO in the visible light region [50].

The optical band gap energy of all samples was estimated using the Tauc equation given below [7]:

$$(\alpha h\nu)^2 = A\left(h\nu - E_g\right) \tag{6}$$

where α is the absorption coefficient, $h\nu$ is the photon energy of incident light, A is a constant and E_g is the optical band gap energy. Figures 9 and 10 show $(\alpha h\nu)^2$ versus $h\nu$ plots of as the prepared samples. The optical band gap energy was estimated by extrapolating the linear part of the curves to the x-axis [7]. The estimated band gap value of undoped CuO was 1.15 eV and increased to 1.25, 1.30, and 1.40 eV for CuO-Fe1, CuOFe-3 and CuO-Fe5, respectively (Fig. 9). The observed increase in the optical band gap energy might be attributed to the Burnstein-Moss effect. When CuO was doped with the iron atoms, electrons of the dopant atom might fill the conduction band states, pushing the Fermi level to the higher energy states [51, 52]. According to the Burnstein-Moss theory, the lifting of the Fermi energy level into the conduction band of the material gives rise to the band gap broadening, known as the blue shift [51, 52].

The estimated values of the optical band gap for CuO-Fe3/Pani(80/20), CuO-Fe3/Pani(60/40), CuO-Fe3/Pani(40/60) and CuO-Fe3/Pani(20/80) were 1.40, 2.00, 2.25 and 2.40 eV, respectively (Fig. 10). The results revealed that the

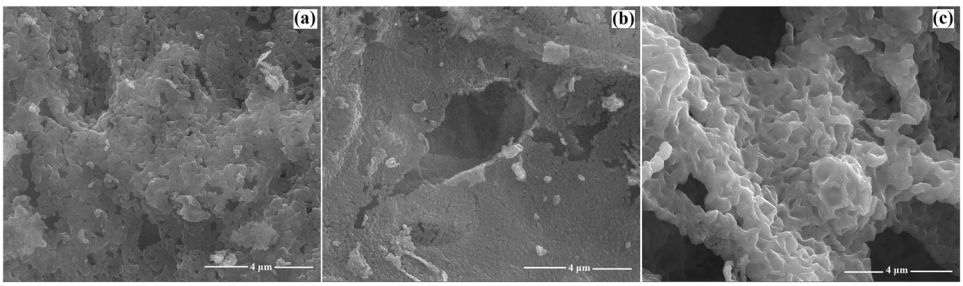

Fig. 7 Morphology analysis: SEM images of the four times of recycled **a** CuO, **b** CuO–Fe3 and **c** CuO–Fe3/Pani(80/20)

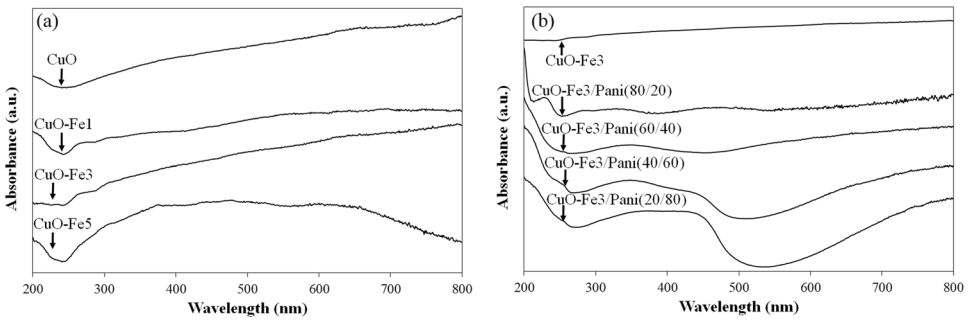

Fig. 8 Optical property analysis: UV–Vis absorption spectrum of **a** CuO–Fe and **b** CuO–Fe3/Pani

composites possessed wider band gap compared to CuO-Fe3. As polyaniline content of the composites increased, the optical band gap continued to expand [52].

5.7 Photocatalytic dye degradation activity

The absorbance of methylene blue with CuO-Fe was lower than that of undoped CuO (Fig. S1). Figure 11a illustrates the photocatalytic degradation of methylene blue with time in the presence of the iron doped CuO nanoparticles. At the end of 240 min of visible light irradiation, the degradation rate of pure CuO, CuO-Fe1, CuO-Fe3 and CuO-Fe5 was 46.0, 49.5, 62.9 and 60.5%, respectively. The iron doping seemed to be beneficial in terms of increasing the photocatalytic efficiency. The highest degradation was obtained with CuO-Fe3. Cu^{2+} ions might be replaced by the Fe^{2+} ions, which might result in an expansion in the crystal lattice of CuO due to the difference between the ionic radii of Cu^{2+} (0.73 Å) and Fe^{2+} (0.78 Å) [7, 53]. The specified lattice expansion might suppress the recombination of the photoexcited charge carriers. In addition, the iron atom might behave as electron traps (Fig. 12a), suppressing the recombination rate of the photoinduced charge carriers on CuO [7]. In the literature, metal or non-metal doping

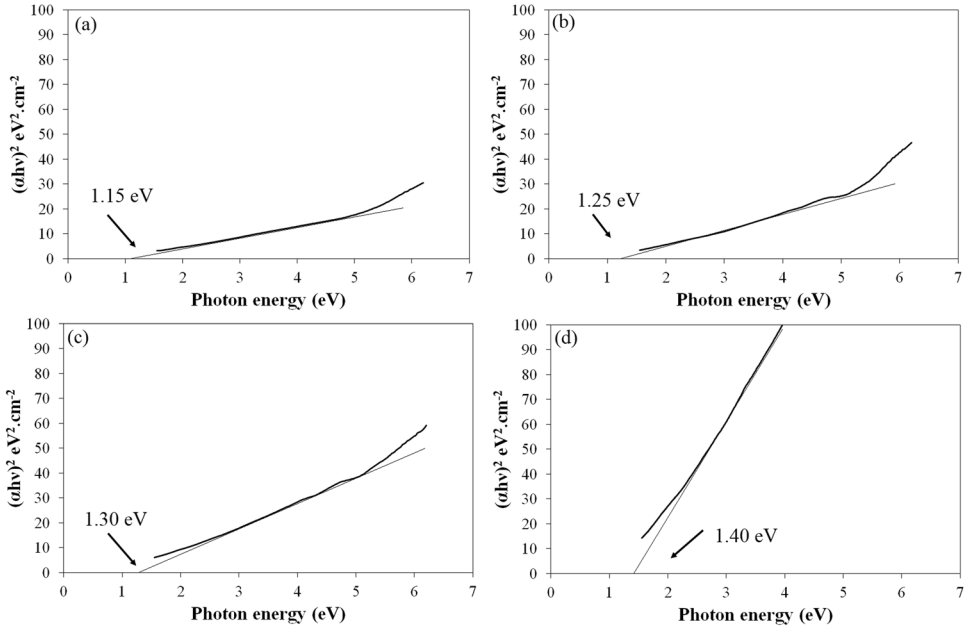

Fig. 9 Optical property analysis: Tauc's plot for **a** CuO, **b** CuO–Fe1, **c** CuO-Fe3 and **d** CuO-Fe5

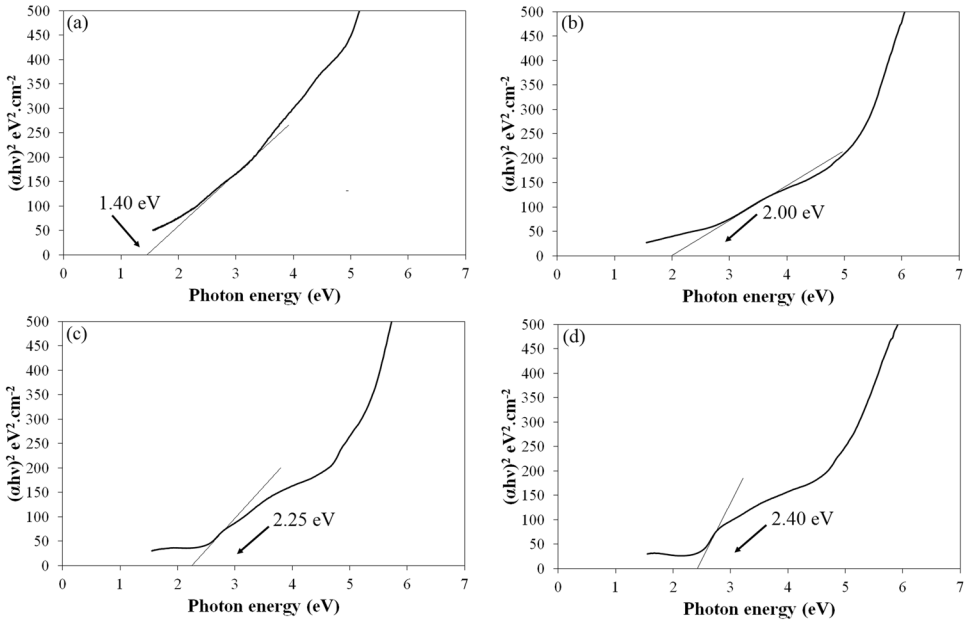

Fig. 10 Optical property analysis: Tauc's plot for **a** CuO–Fe3/Pani(80/20), **b** CuO–Fe3/Pani(60/40), **c** CuO–Fe3/Pani(40/60) and **d** CuO–Fe3/Pani(20/80)

provided almost 10–20% enhancement in the photocatalytic dye degradation efficiency within 240 min under visible light irradiation. George and his coworkers improved the dye removal rate from 42 to 60% within 240 min [18]. Compared with studies in the literature (Table 1), a significant improvement of almost 20% in the photocatalytic dye degradation efficiency was achieved with the iron doping.

Methylene blue with the CuO-Fe3/Pani(80/20) and CuO-Fe3/Pani(60/40) composites exhibited lower absorption peaks compared to CuO-Fe3, which indicated that combining CuO-Fe3 with Pani has been found to be successful in terms of the photocatalytic activity (Fig. S2). Figure 11b exhibits the graph for degradation rate of methylene blue with the CuO-Fe3/Pani composites under the visible light. The photocatalytic degradation rate of methylene blue was about 71.9, 69.6, 48.8 and 34.8%, when the CuO-Fe3/Pani(80/20), CuO-Fe3/Pani (60/40), CuO-Fe3/Pani(40/60) and CuO-Fe3/Pani(20/80), respectively, were used as photocatalysts under the visible light irradiation. When compared with CuO-Fe3, the CuO-Fe3/Pani(80/20) and CuO-Fe3/Pani(60/40) composites provided higher photocatalytic degradation activity. Because of the difference between the band potentials (Fig. 12b), combining CuO-Fe3 nanoparticles with polyaniline in the composite structure might cause the photoexcited electrons to move from the con-

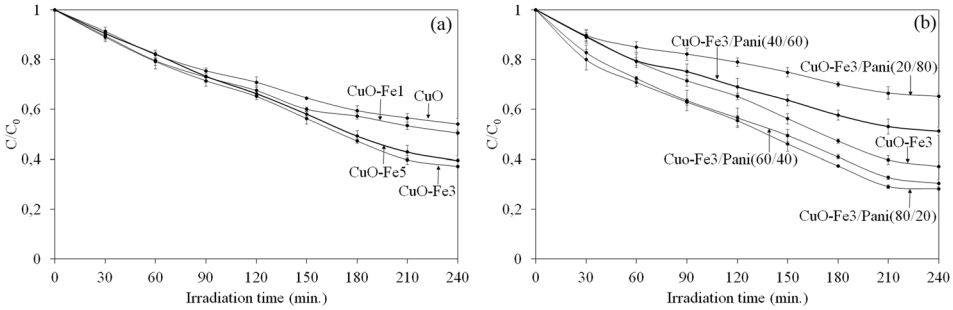

Fig. 11 Photocatalytic activity measurement: Photocatalytic degradation rate of methylene blue in the presence of **a** CuO–Fe and **b** CuO–Fe3/Pani

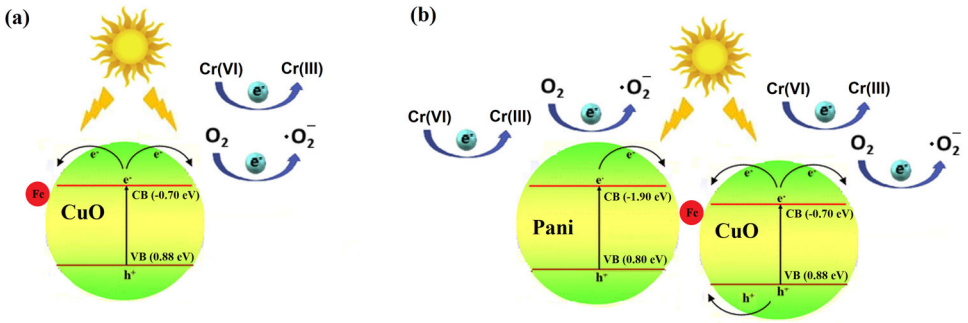

Fig. 12 Photocatalytic activity mechanism: Proposed photocatalytic dye degradation and Cr(VI) photoreduction mechanisms of **a** CuO–Fe and **b** CuO–Fe3/Pani

Table 1 Comparison with previous reports of CuO doped with metal or non-metal atoms

Dopant atom	Light source	Dye removal rate of CuO	Dye removal rate of doped CuO
Ce (0.6 mM) [7]	Xe lamp (800 > λ > 200 nm)	~76% in 240 min.	90.4% in 240 min.
La (5.78 wt.%) [6]	Xe lamp (800 > λ > 200 nm)	~79.4% in 240 min.	~90.9% in 240 min.
Ag (4 wt.%) [10]	Xe lamp (300 W)	~40% in 40 min.	~65% in 60 min.
Li (5 mol.%) [11]	Tungsten lamp (300 W)	~86% in 120 min.	~93% in 120 min.
Ca (1.38 at.%) [12]	Xe lamp (800 > λ > 200 nm)	84.26% in 240 min.	92.33% in 240 min.
Mn (2 wt.%) [13]	UV-Visible light	~79% in 480 min.	~87% in 480 min.
Fe (0.01 mol) [5]	Visible light	-	~62% in 60 min.
Fe [18]	Hg lamp (50 W)	~42% in 240 min.	~60% in 240 min.
N [19]	Visible light (λ > 420 nm)	-	~80% in 75 min.
C [20]	Xe lamp (150 W)	~70% in 240 min.	~90% in 240 min.

duction band of Pani (−1.90 eV) to the conduction band of CuO-Fe3 (−0.70 eV) [54, 55]. At the same time, the photoinduced holes of CuO-Fe3 might transfer to the valence band of Pani. Because of the delocalized π-conjugated structures, polyaniline has high electron transfer ability, leads to fast charge separation on polyaniline [56]. Hence, the recombination rate of the photoexcited electron-pairs might be reduced at a certain extent. On account of promoting the separation of the photoinduced charge carriers, higher photocatalytic efficiency was obtained with the CuO-Fe3/Pani(80/20) and CuO-Fe3/Pani(60/40) composites compared to CuO-Fe3. The same effect could not be achieved with the CuO-Fe3/Pani(40/60) and CuO-Fe3/Pani(20/80) composites. The specified composites have high Pani content and the CuO-Fe3 nanoparticles might be covered with a dense polymer layer. Photocatalytic activity takes place on the photocatalyst surface [57]. It was thought that Pani layers covering the CuO-Fe3 nanoparticles might reduce the contact surface area of the photocatalyst with the methylene blue molecules, resulting in a lower degradation efficiency compared to CuO-Fe3. According to these results, the content of the conductive polymer in the composite structure should be kept limited.

The reaction rate constant values, obtained from Fig. S3a and b, are listed in Table 2. According to Table 2, the iron doped CuO nanoparticles had higher k values than that of undoped CuO. According to the literature, the value of the reaction rate constant for the iron doped CuO was 1.5 times higher than that of undoped CuO [5]. A similar 1.5-fold increase was observed in the reaction rate constant value. Among the composites, CuO-Fe3/Pani(80/20), CuO-Fe3/Pani(60/40) and CuO-Fe3/Pani(40/60) provided higher k values compared to undoped CuO. The highest k value obtained by the CuO-Fe3/Pani(80/20) composite was almost 1.9 times as high as that of undoped CuO. High R^2 values close to 1 indicated the compatibility of the dye degradation data with the pseudo-first-order kinetic model.

Table 2 Adjusted parameters of the pseudo-first-order kinetic model

Sample	k (min^{-1})	R^2
CuO	0.0028	0.9848
CuO-Fe1	0.0031	0.9776
CuO-Fe3	0.0041	0.9886
CuO-Fe5	0.0038	0.9908
CuO-Fe3/Pani(80/20)	0.0054	0.9870
CuO-Fe3/Pani(60/40)	0.0050	0.9926
CuO-Fe3/Pani(40/60)	0.0030	0.9859
CuO-Fe3/Pani(20/80)	0.0019	0.9597

5.8 Real wastewater and reusability study

In order to examine the effects of real wastewater environment on the photocatalytic activity, the photocatalytic degradation of methylene blue added into a real wastewater sample was also studied. The degradation rate of methylene blue solutions prepared using distilled water and real wastewater in the presence CuO was 46.0 and 37.8%, respectively, in 240 min (Fig. 13a). When a real wastewater was used instead of distilled water to prepare the methylene blue solution, 59.2% dye degradation was obtained in the presence of CuO-Fe3 (Fig. 13a). The degradation rate of the model dye solution prepared using distilled water and real wastewater by CuO-Fe3/Pani(80/20) was 71.9 and 66.9%, respectively, in 240 min (Fig. 13a). According to these results, the photocatalytic activity of the noticed samples reduced in the methylene blue solution prepared using the real wastewater. The greatest reduction about 18% was found in the photocatalytic dye degradation of undoped CuO. The decrease in the photocatalytic efficiency was attributed to the decrease in the effective surface area required for dye degradation. It was thought that the pollution in the wastewater adsorbed to the photocatalyst surface, reducing the required surface area for the photocatalytic degradation reaction.

The stability of the as-prepared photocatalysts was studied through the reusability test. The photocatalytic degradation rate of methylene blue for four times of recycled CuO, CuO-Fe3 and CuO-Fe3/Pani(80/20) was 29.1, 41.9 and 55.3%, respectively after 240 min (Fig. 13b). CuO, CuO-Fe3 and CuO-Fe3/Pani(80/20) retain 63.2, 66.5 and 76.9% of its photocatalytic activity, respectively, at the 4th catalytic cycle. The highest photocatalytic activity among

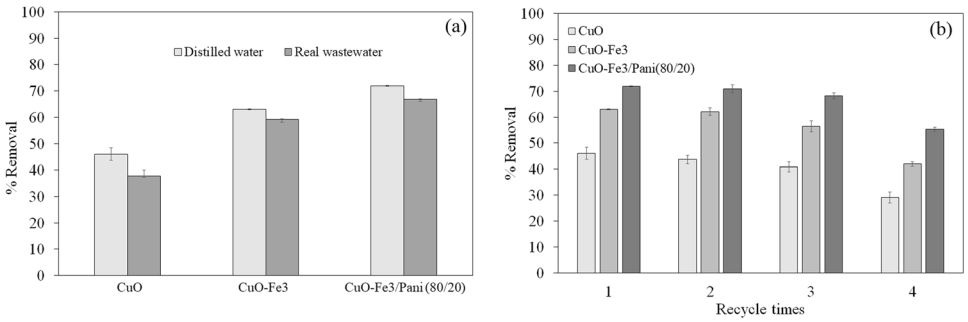

Fig. 13 Photocatalytic activity measurement: **a** Photocatalytic removal rate of methylene blue prepared using distilled water and real wastewater, **b** reusability study of the recovered photocatalysts

four times of recycled samples was obtained with the CuO-Fe3/Pani(80/20) composite, indicating that CuO compounded with a polymer matrix had a better reusability compared to pure CuO. In addition, the composite sample could be recycled more easily compared to pure CuO nanoparticles. The reduction in the photocatalytic dye degradation rate might be due to the intermediate products adsorbed to the surface of the photocatalyst nanoparticles. The intermediate products might block the active sites of the photocatalyst nanoparticles and might not be removed from the photocatalyst surface during rinsing with distilled water [48].

5.9 Effect of scavengers on the photocatalytic activity

Under the visible light irradiation, electrons from the valence band of CuO could be excited to its conduction band, which gave rise to the formation of holes in the valence band (7). The photoinduced electron-hole pairs could move to the surface of CuO, where they could participate in the photocatalytic degradation reaction. The photoinduced electrons could react with surface adsorbed O_2 molecules to form superoxide ($\cdot O_2^-$) radicals (8) and the photoinduced holes could react with surface adsorbed water molecules to form ·OH radicals (9).

$$CuO + hv \rightarrow e^- + h^+ \quad (7)$$

$$O_2 + e^- \rightarrow \cdot O_2^- \quad (8)$$

$$H_2O + h^+ \rightarrow \cdot OH + H^+ \quad (9)$$

The reduction potential of O_2 to form superoxide radical, which is −0.33 eV vs. NHE, is more positive than the conduction band potential of CuO (−0.70 eV) [54, 58]. Hence, the photoexcited electrons of CuO could reduce the surface adsorbed O_2 molecules to the superoxide radicals. The superoxide radicals could decompose the organic dye molecules (10) [1]:

$$\cdot O_2^- + \text{organic dye} \rightarrow \text{degradation products} \quad (10)$$

Alternatively, the superoxide radicals could be reduced by the photoexcited electrons of CuO to H_2O_2 (11), which could also be reduced to hydroxyl radicals since the redox potential of the H_2O_2/·OH couple (0.38 eV) is more positive than the conduction band potential of CuO (12) [59]. The conduction band potential of CuO is more negative than the reduction potential of $\cdot O_2^-$ to form H_2O_2, which is 0.695 eV vs. NHE [60].

$$\cdot O_2^- + 2H^+ + e^- \rightarrow H_2O_2 \quad (11)$$

$$H_2O_2 + H + e^- \rightarrow H_2O + \cdot OH \quad (12)$$

In order to visualize the degradation effect of the superoxide radical, $\cdot O_2^-$ scavenger was added into the reaction medium of CuO and CuO-Fe3, separately. The photocatalytic degradation efficiency of CuO and CuO-Fe3 for methylene blue with $\cdot O_2^-$ scavenger was found to be 21.6 and 33.9%, respectively (Fig. 14a, b). There was a significant decrease in the photocatalytic activity of the specified photocatalysts. This showed that the superoxide radicals had an important role in the photocatalytic degradation of methylene blue. The greatest reduction in the photocatalytic activity was observed by CuO-Fe3 (Fig. 14b).

Because the redox potential of the couple H_2O/·OH, which is 2.27 eV vs. NHE, is more positive than the valence band potential of CuO (0.88 eV), surface adsorbed H_2O molecules could not be oxidized by the photoexcited holes of CuO to form ·OH radicals [54, 58]. The possible involvement of ·OH radicals in the photocatalytic degradation reaction was investigated by the trapping experiment using ·OH radical scavenger (Fig. 14a, b). The photocatalytic degradation rate of methylene blue for CuO and CuO-Fe3 decreased from 46.0, 62.9 to 44.7, 61.1%, respectively after 240 min. There was a slight decrease in the degradation values, indicating the inactiveness of the hydroxyl radical. Since the H_2O/·OH redox potential is higher than the valence band of CuO, the generation of the hydroxyl radical from H_2O on the valence band of CuO seemed to be impossible. The hydroxyl scavenger test results supported this statement. The reason for the slight decrease in the degradation efficiency might be the hydroxyl radical,

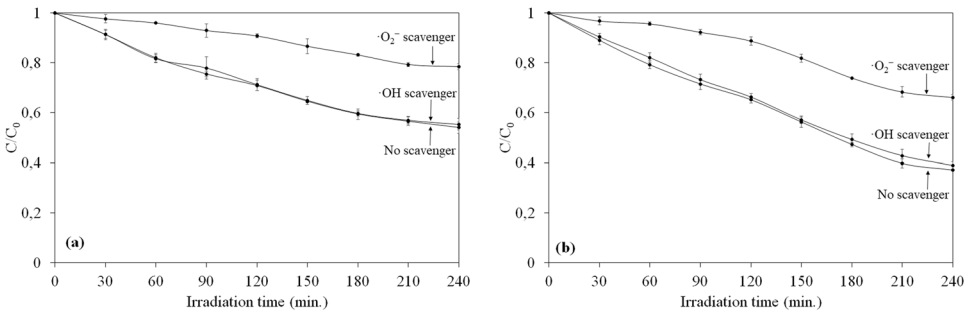

Fig. 14 Photocatalytic activity measurement: Photocatalytic degradation rate of methylene blue with superoxide radical scavenger and hydroxyl radical scavenger, separately, in the presence of **a** CuO and **b** CuO–Fe3

formed through the reduction reaction of H_2O_2 on the conduction band of CuO (12) [59]. Hence, the superoxide radical might the only reactive species, which participated actively in the photocatalytic degradation of methylene blue.

5.10 Effect of pH on the photocatalytic activity

Wastewater, including organic dye solutions, can have different pH values, and acidic or basic pH values can change the surface charge of the photocatalyst, which might affect the electrostatic interaction between the dye molecules and the photocatalyst. The difference in surface charges might also affect the adsorption ability of the photocatalyst. Since the redox potentials of radical formation change depending on the pH of the reaction medium, a marked change in the formation rate of superoxide and hydroxide radical can also be expected [48]. When the pH of the reaction medium was higher than 7, the pH of the solution might be above CuO's point of zero charge [48]. Hence, the surface of both undoped and doped CuO might become negatively charged, enhancing the electrostatic attraction between CuO and the positively charged methylene blue molecules [34]. According to Fig. 15a–c, the photocatalytic degradation rate of methylene blue for CuO, CuO-Fe3, CuO-Fe3/Pani(80/20) increased from 46.0, 62.9, 71.9% to 53.8, 76.0, 79.2%, respectively, after 240 min of the visible light irradiation at pH = 10. It was observed that the possible improvement in the electrostatic interaction at high pH value promoted the photocatalytic degradation efficiency.

On the other hand, the photocatalytic degradation rate of methylene blue for CuO, CuO-Fe3, CuO-Fe3/Pani(80/20) decreased from 46.0, 62.9, 71.9% to 34.9, 51.8, 69.6%, respectively, within 240 min at pH = 4 (Fig. 15a–c). When the pH of the methylene blue solution was acidic, the pH of the solution might be below CuO's point of zero charge [48]. Thus, the surface of the photocatalyst nanoparticles, CuO and CuO-Fe3, might become positively charged, suppressing the electrostatic attraction between the photocatalyst nanoparticles and the positively charged dye molecules, and also the photocatalytic degradation efficiency. In addition, CuO nanoparticles might react with the acid molecules to generate its salt in the acidic pH, which might also reduce the formation of $\cdot O_2^-$ radicals on the surface of CuO and the photocatalytic degradation efficiency [48]. The photocatalytic activity of the CuO-Fe3/Pani(80/20) composite reduced in the acidic pH value and improved in the basic pH value. Pani in the composite structure did not alter the pH dependent photocatalytic behavior of CuO.

5.11 Effect of H_2O_2 on the photocatalytic activity

Hydrogen peroxide, which is a strong oxidative chemical, has been utilize to reduce both chemical oxygen demand and biological oxygen demand in wastewater. In addition, hydrogen peroxide has been utilized to improve the existing physical or biological wastewater treatment processes. H_2O_2 is a chemical with a high probability of being present in the solution environment as a reaction intermediate of the photocatalytic dye degradation reactions. In order to study the effects of ambient conditions on the photocatalytic activity of CuO, H_2O_2 was added into the methylene blue solution. When the photocatalyst samples, CuO, CuO-Fe3 and CuO-Fe3/Pani(80/20), were used in combination with H_2O_2, the degradation rate of methylene blue increased slightly (Fig. 15d). The conduction band potential of CuO (−0.70 eV) is more negative than the reduction potential of H_2O_2 (0.38 eV) to form hydroxyl radicals (12) [59]. Hence, H_2O_2 molecules could be reduced on the conduction band of CuO with the photoinduced electrons to form additional hydroxyl radicals, which could decompose the organic dye molecules into small harmless molecules. In addition, H_2O_2 is a good electron acceptor, which provides it a high reduction tendency on the CuO surface [1]. According to Fig. 15d, addition of a small amount H_2O_2 into the reaction medium seemed to effective in terms of the photocatalytic degradation efficiency. The photocatalytic degradation efficiency of CuO, CuO-Fe3 and CuO-Fe3/Pani(80/20) for methylene blue with H_2O_2 (l mg/ml) were found to be 49.6, 72.9 and 87.6%, respectively, at 240 min. The degradation efficiency of the CuO-Fe3/Pani(80/20) composite for methylene blue increased almost 16%.

5.12 Effect of the intial dye concentration and the photocatalyst loading on the photocatalytic activity

The intial dye concentration is an important parameter in the wastewater treatment. In this context, the effect of the intial dye concentration (10, 20, 30 and 40 mg/l) on the photocatalytic activity of the CuO-Fe3/Pani(80/20) composite was studied. According to Fig. 16a, the photocatalytic dye degradation efficiency of CuO-Fe3/Pani(80/20) composite decreased as the initial dye concentration increased. When the initial dye concentration changed from 10 to 40 mg/l, the dye removal rate decreased from 71.9 to 50.7%. When the initial dye concentration increases, the amount of dye molecules adsorbed on the photocatalyst surface also increases, preventing the photocatalyst from absorbing photons and reducing the photocatalytic dye degradation efficiency [61]. The photocatalyst content of the dye solution is another important parameter influencing the phtocatalytic dye degradation efficiency. According to Fig. 16b, the photocatalytic dye degradation efficiency of the CuO-Fe3/Pani(80/20) composite enhanced from 63.3 to 76.9% when the catalyst content of the dye solution increased from 0.25 to 0.75 g/l. Then, there was a slight decrease in dye

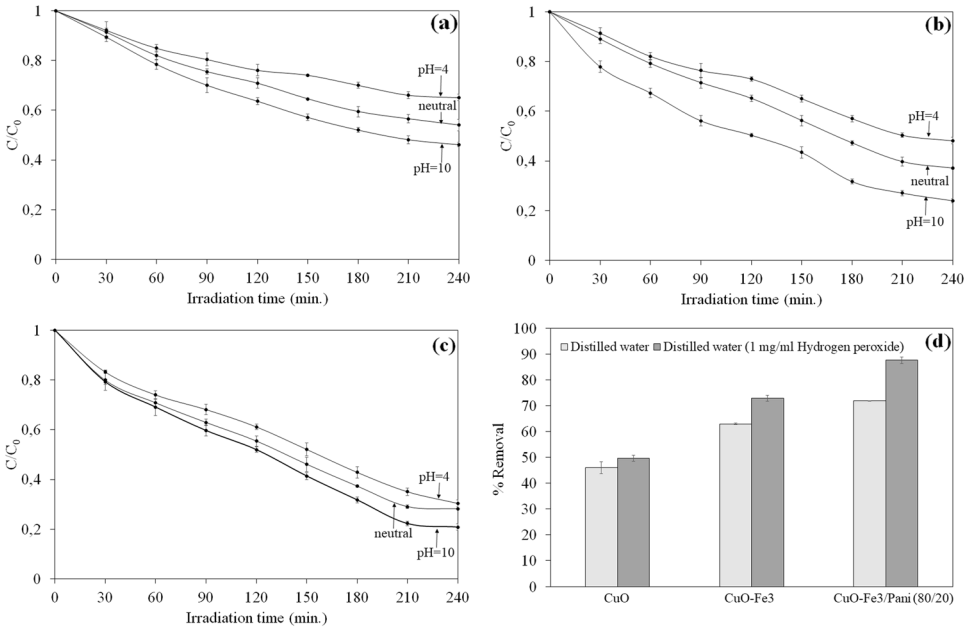

Fig. 15 Photocatalytic activity measurement: Effect of pH on the photocatalytic degradation rate of methylene blue in the presence of **a** CuO, **b** CuO–Fe3, **c** CuO–Fe3/Pani(80/20), **d** effect of H_2O_2 on the photocatalytic degradation rate of methylene blue in the presence of CuO, CuO-Fe3 and CuO/Fe3/Pani, respectively

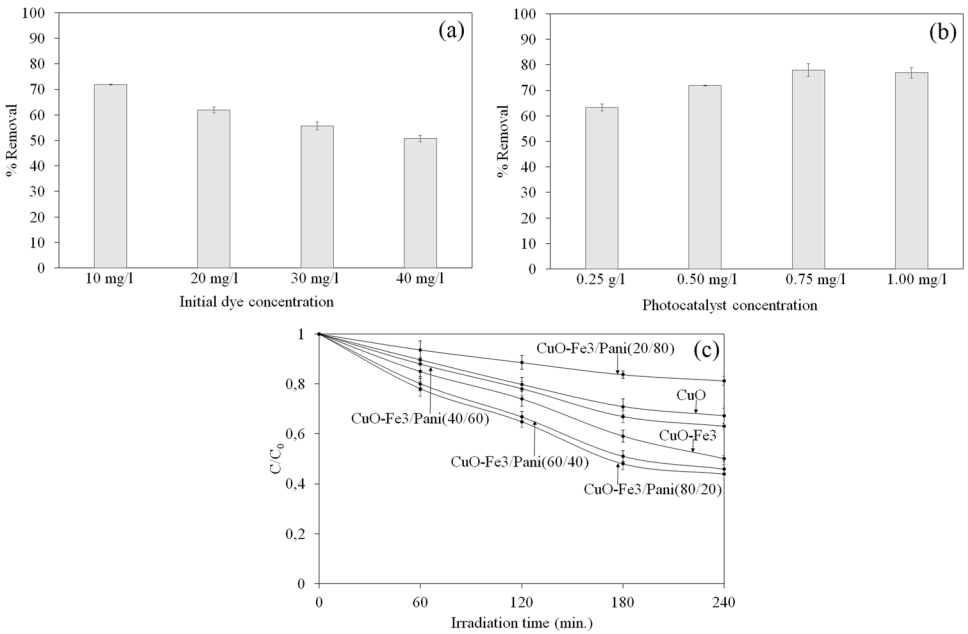

Fig. 16 Photocatalytic activity measurement: **a** The photocatalytic dye degradation rate of CuO–Fe3/Pani(80/20) with different initial solution concentration of methylene blue, **b** effect of the photocatalyst (CuO–Fe/Pani(80/20)) concentration on the photocatalytic dye degradation rate, **c** the Cr(VI) photoreduction rate of CuO, CuO–Fe3, CuO–Fe3/Pani under visible light irradiation

degradation efficiency as the photocatalyst content continued to increase to 1.0 g/l. When the photocatalyst concentration of the dye solution is dilute, the photocatalyst can absorb fewer photons required for the photocatalytic activity, leading to low efficiency. Increasing the photocatalyst concentration leads to an enhancement in photocatalytic activity due to the increase in the photon absorption ability. However, after a certain concentration, the photocatalyst may block the light transmittance of the dye solution, leading to a decrease in the photocatalytic dye degradation efficiency [61]. Accordingly, increasing the photocatalyst concentration too much causes not only a catalyst waste, but also a reduced photocatalytic activity.

5.13 Photocatalytic reduction of Cr(VI)

Fig. S4 exhibits absorbance changes of Cr(VI) in the presence of the as-prepared samples. It was noticed from Fig. 16c that CuO-Fe3 exhibited enhanced photoreduction performance than that of pure CuO. 32.8% and 49.9% of Cr(VI) was reduced within 240 min by CuO and CuO-Fe3, respectively. In the literature, there is no study on the Cr(VI) photoreduction

of pure CuO or doped CuO. Metal atom doping was applied to CuO heterojunction structures [21, 22] Within this scope, Udayabhanu and his coworkers obtained 55% Cr(VI) removal rate with Cu doped TiO_2/CuO heterojunction structure in 240 min. Compared with the CuO studies in the literature, the photoreduction rate of Cr(VI) was increased by about 20%, and a significant value of approximately 50% Cr(VI) removal rate was obtained with the iron doped CuO [21, 22]. After 240 min of the visible light irradiation, the Cr(VI) photoreduction rate of CuO-Fe3/Pani(80/20), CuO-Fe3/Pani(60/40), CuO-Fe3/Pani(40/60) and CuO-Fe3/Pani(20/80) was 56.1, 54.1, 37.0 and 18.7%, respectively (Fig. 16c) Obviously, the Cr(VI) photoreduction efficiency of the CuO-Fe3/Pani composites decreased with increasing the Pani content of the composite. The optimized composition of CuO-Fe3 in the composites was 80%. The conducting polymer might block the active surface required for the Cr(VI) photoreduction reaction. According to the Cr(VI) photoreduction results, combining CuO-Fe3 in the composite structure with the conducting polymer was beneficial in terms of the photoreduction efficiency. However, the Pani phase of the composite should be the minority phase to take advantage of the synergy effect of the composite. The possible Cr(VI) photoreduction mechanism was also illustrated in Fig. 12. Since the reduction potential of the Cr(VI)/Cr(III) couple (1.33 eV vs. NHE) is more positive than the conduction band potential of both CuO and Pani, the photogenerated electrons of both CuO-Fe3 and Pani might reduce the Cr(VI) ions according to the following reaction (13) [57]:

$$Cr_2O_7^{2-} + 14H^+ + 6e^- \rightarrow 2Cr^{3+} + 7H_2O \quad (13)$$

Doping CuO with the iron atom and coupling it with Pani enhanced the Cr(VI) photoreduction rate, which might be due to the suppression in the recombination of the photoexcited charge carriers.

6 Conclusion

In summary, the solution combustion technique was applied to prepare undoped CuO and the iron doped CuO nanoparticles. The photocatalytic dye degradation experiments revealed that the iron atom doping induced a blue shift of the light absorption. The addition of the iron atoms enhanced both the photocatalytic dye degradation efficiency and the Cr(VI) photoreduction efficiency of CuO under the visible light irradiation. The improved photocatalytic activity of doped CuO was attributed to the electron trapping ability of the dopant atom. Based on the radical scavenger experiments, superoxide radicals were considered to be the active species in the photocatalytic dye degradation reaction. The CuO-Fe3/Pani(80/20) composite was exhibited to be highly recyclable up to four consecutive cycles with a 22.1% loss in the dye degradation efficiency. The use of real wastewater instead of distilled water to prepare the dye solution slightly affected the photocatalytic activity of the as-prepared samples. Hydrogen peroxide added into the reaction medium improved the dye degradation efficiency of the prepared photocatalyst samples. Within the scope of this study, the potential for use of CuO as a photocatalyst has been increased by doping with a metal atom and compounding with a conducting polymer.

Data availability

The data that support the findings of this study are available from the corresponding author upon reasonable request.

Author contributions All authors contributed to the study conception and design. Material preparation, data collection and analysis were performed by OK and HNK. The first draft of the manuscript was written by OK and HNK. They read and approved the final manuscript.

Funding This research has been supported by Ankara University Scientific Research Projects Coordination Unit. Project Number: 22H0443001, 2022.

Compliance with ethical standards

Conflict of interest The authors declare no competing interests.

References

1. Mageshwari K, Sathyamoorthy R, Park J (2015) Photocatalytic activity of hierarchical CuO microspheres synthesized by facile reflux condensation method. Powder Technol 278:150–156
2. Batista APL, Carvalho HWP, Luz GHP, Martins PFQ, Gonçalves M, Oliveira LCA (2010) Preparation of CuO/SiO_2 and photocatalytic activity by degradation of methylene blue. Environ Chem Lett 8:63–67
3. Dong GH, Zhang LZ (2013) Synthesis and Enhanced Cr(VI) Photoreduction Property of Formate Anion Containing Graphitic Carbon Nitride. J Phys Chem C 117(8):4062–4068
4. Nezamzadeh-Ejhieh A, Karimi-Shamsabadi M (2014) Comparison of photocatalytic efficiency of supported CuO onto micro and nano particles of zeolite X in photodecolorization of Methylene blue and Methyl orange aqueous mixture. Appl Catal A-Gen 477:83–92
5. Zhu JF, Xiao Q (2015) Meso-macroporous Fe-doped CuO: Synthesis, characterization, and structurally enhanced adsorption and visible-light photocatalytic activity. J Cent South Univ 22:4105–4111
6. Yan B, Wang Y, Jiang T, Wu X (2016) Synthesis and enhanced photocatalytic property of La-doped CuO nanostructures by electrodeposition method. J Mater Sci: Mater Electron 27:5389–5394
7. Chen YJ, Tan HW, Wu XQ, Sun QM, Wang DG, Wang YQ (2019) Effect of Doping Ce Ions on Morphology and Photocatalytic Activity of CuO Nanostructures. Cryst Res Technol 54:1900033
8. Li Y, Yang F, Yu Y (2017) LSDA plus U study on the electronic and anti-ferromagnetic properties of Ni-doped CuO and Cu-doped NiO. Chin J Catal 38:767–774

9. Andrade Neto NF, Oliveira PM, Paskocimas CA, Bomio MRD, Motta FV (2019) Enhanced Photocatalytic Properties of Zinc-Doped CuO Decorated with Silver Obtained by Microwave-Assisted Hydrothermal Method: Statistical Factorial Design. J Electron Mater 48:4840–4849
10. Iqbal S, Javed M, Bahadur A, Qamar MA, Ahmad M, Shoaib M, Raheel M, Ahmad N, Akbar MB, Li H (2020) Controlled synthesis of Ag-doped CuO nanoparticles as a core with poly(acrylic acid) microgel shell for efficient removal of methylene blue under visible light. J Mater Sci: Mater Electron 31:8423–8435
11. Siddiqui H, Qureshi MS, Haque FZ (2021) Lithium-Doped CuO Nanosheets: Structural Transformation, Optical, and Electrical Characteristics with Enhanced Photocatalytic and Solar Cell Performance. Energy Environ Mater 4:646–657
12. Wang YQ, Jiang TT, Meng DW, Wang DG, Yu MH (2015) Synthesis and enhanced photocatalytic property of feather-like Cd-doped CuO nanostructures by hydrothermal method. Appl Surf Sci 355:191–196
13. Iqbal M, Thebo AA, Shah AH, Iqbal A, Thebo KH, Phulpoto S, Mohsin MA (2017) Influence of Mn-doping on the photocatalytic and solar cell efficiency of CuO nanowires. Inorg Chem Commun 76:71–76
14. Shaghaghi Z, Amani-Ghadim AR, Seraji M (2020) Structural properties and photocatalytic degradation efficiency of CuO and erbium doped CuO nanostructures prepared by thermal decomposition of some Cu-salophen type complexes as precursors. Mater Chem Phys 243:122635
15. Maraj M, Raza A, Wang X, Chen J, Riaz KN, Sun W (2021) Mo-Doped CuO Nanomaterial for Photocatalytic Degradation of Water Pollutants under Visible Light. Catalysts 11:1198
16. Hao JJ, Xie L, Zhang YX, Xing ST (2021) Enhanced degradation of sulfamethoxazole by peroxydisulfate activation with Mg-doped CuO. Desalin Water Treat 231:254–262
17. Pugazhendhi A, Kumar SS, Manikandan M, Saravanan M (2018) Photocatalytic properties and antimicrobial efficacy of Fe doped CuO nanoparticles against the pathogenic bacteria and fungi. Micro Pathog 122:84–89
18. George A, Raj DMA, Venci X, Raj AD, Irudayaraj AA, Josephine RL, Sundaram SJ, Al-Mohaimeed AM, Al Farraj DA, Chen TW (2022) Photocatalytic effect of CuO nanoparticles flower-like 3D nanostructures under visible light irradiation with the degradation of methylene blue (MB) dye for environmental application. Environ Res 203:111880
19. Ardekani SR, Rouhaghdam AS, Nazari M (2018) N-doped ZnO-CuO nanocomposite prepared by one-step ultrasonic spray pyrolysis and its photocatalytic activity. Chem Phys Lett 705:19–22
20. Hosseini SMH, Moakhar RS, Soleimani F, Sadrnezhaad SK, Masudy-Panah S, Katal R, Seza A, Ghane N, Ramakrishna S (2020) One-pot microwave synthesis of hierarchical C-doped CuO dandelions/g-C_3N_4 nanocomposite with enhanced photostability for photoelectrochemical water splitting. Appl Surf Sci 530:147271
21. Li JW, Guo JS, Zhang JX, Sun ZL, Gao JP (2022) Surface etching and photodeposition nanostructures core-shell Cu_2O@CuO-Ag with S-scheme heterojunction for high efficiency photocatalysis. Surf Interfaces 34:102308
22. Udayabhanu RNL, Shankar MV, Sharma SC, Nagaraju G (2020) One-pot synthesis of Cu-TiO_2/CuO nanocomposite: Application to photocatalysis for enhanced H_2 production, dye degradation & detoxification of Cr(VI). Int J Hydrog Energy 45(13):7813–7828
23. Rajendran S, Pachaiappan R, Hoang TKA, Karthikeyan S, Gnanasekaran L, Vadivel S, Soto-Moscoso M, Gracia-Pinilla MA (2021) CuO-ZnO-PANI a lethal p-n-p combination in degradation of 4-chlorophenol under visible light. J Hazard Mater 416:125989
24. Asgari E, Esrafili A, Jafari AJ, Kalantary RR, Farzadkia M (2019) Synthesis of TiO_2/polyaniline photocatalytic nanocomposite and its effects on degradation of metronidazole in aqueous solutions under UV and visible light radiation. Desalin Water Treat 161:228–242
25. Faisal M, Harraz FA, Ismail AA, Alsaiari MA, Al-Sayari SA, Al-Assiri MS (2019) Novel synthesis of Polyaniline/$SrSnO_3$ nanocomposites with enhanced photocatalytic activity. Ceram Int 45:20484–20492
26. Sahu K, Rahamn KH, Kar AK (2019) Synergic effect of polyaniline and ZnO to enhance the photocatalytic activity of their nanocomposite. Mater Res Express 6:095304
27. Jia XC, Jiang DH, Gouma PI (2022) Facile synthesis of self-supported WO_3/PANI hybrid photocatalyst for methylene blue degradation under visible light. Mater Lett 314:131869
28. Ghaly HA, El-Kalliny AS, Gad-Allah TA, Abd El-Sattar NEA, Souaya ER (2017) Stable plasmonic Ag/AgCl–polyaniline photoactive composite for degradation of organic contaminants under solar light. RSC Adv 7:12726–12736
29. Wang J, Hao XY, Jiang YX, Zhang DE, Ren LZ, Gong JY, Wu XJ, Zhang YY, Tong ZW (2019) Synthesis, structure, and photocatalytic activity of PANI/BiOCl nanocomposites. Mater Res Express 6:0850c1
30. Singh SJ, Chinnamuthu P (2021) Highly efficient natural-sunlight-driven photodegradation of organic dyes with combustion derived Ce-doped CuO nanoparticles. Colloid Surf A-Physicochem Eng Asp 625:126864
31. Sedenkova I, Konyushenko EN, Stejskal J, Trchova M, Prokes J (2011) Solid-state oxidation of aniline hydrochloride with various oxidants. Synth Met 161:1353–1360
32. Stejskal J, Gilbert RG (2002) Polyaniline. Preparation of a Conducting Polymer. Pure Appl Chem 74:857–867
33. Badvi K, Javanbakht V (2021) Enhanced photocatalytic degradation of dye contaminants with TiO_2 immobilized on ZSM-5 zeolite modified with nickel nanoparticles. J Clean Prod 280:124518
34. Kinoshita M, Shimoyama Y (2018) Photocatalytic activity of mixed-phase titanium oxide synthesized by supercritical sol-gel reaction. J Supercrit Fluids 138:29–35
35. Zeng XL, Sun XZ, Yu YS, Wang HY, Wang Y (2019) Photocatalytic degradation of flumequine with B/N codoped TiO_2 catalyst: Kinetics, main active species, intermediates and pathways. Chem Eng J 378:UNSP122226
36. Xu LH, Su J, Zheng GG, Zhang L (2019) Enhanced photocatalytic performance of porous ZnO thin films by CuO nanoparticles surface modification. Mater Sci Eng B-Adv Funct Solid-State Mater 248:114405
37. Yin HF, Yuan CY, Lv HJ, Zhang KY, Chen X, Zhang YZ (2022) Hierarchical Ti_3C_2 MXene/$Zn_3In_2S_6$ Schottky junction for efficient visible-light-driven Cr(VI) photoreduction. Ceram Int 48(8):11320–11329
38. Bhattacharjee A, Ahmaruzzaman M (2016) CuO nanostructures: Facile synthesis and applications for enhanced photodegradation of organic compounds and reduction of p-nitrophenol from aqueous phase. RSC Adv 6:41348–41363
39. Shafiey Dehaj M, Zamani Mohiabadi M (2019) Experimental study of water-based CuO nanofluid flow in heat pipe solar collector. J Therm Anal Calorim 137:2061–2072
40. Wan Q, Zhang JL, Zhang BX, Tan DX, Yao L, Zheng LR, Zhang FY, Liu LF, Cheng XY, Han BX (2020) Boron-doped CuO nanobundles for electroreduction of carbon dioxide to ethylene. Green Chem 22(9):2750–2754
41. Jundale DM, Navale ST, Khuspe GD, Dalavi DS, Patil PS, Patil VB (2013) Polyaniline–CuO hybrid nanocomposites: Synthesis, structural, morphological, optical and electrical transport studies. J Mater Sci: Mater Electron 24:3526–3535
42. Shao W, Jamal R, Xu F, Ubul A, Abdiryim T (2012) The Effect of a Small Amount of Water on the Structure and Electrochemical

Properties of Solid-State Synthesized Polyaniline. Materials 5:1811–1825
43. Chauhan A, Verma R, Batoo KM, Kumari S, Kalia R, Kumar R, Hadi M, Raslan EH, Imran A (2021) Structural and optical properties of copper oxide nanoparticles: A study of variation in structure and antibiotic activity. J Mater Res 36:1496–1509
44. Sharma S, Singh KL, Kumar M, Prasher S (2022) Structural, Optical and Thermal Properties of PVC/ Polyaniline Composite Thin Films. JOM 74:354–360
45. Kathalingam A, Ramesh S, Yadav HM, Choi JH, Kim HS, Kim HS (2020) Nanosheet-like $ZnCo_2O_4$@nitrogen doped graphene oxide/polyaniline composite for supercapacitor application: Effect of polyaniline incorporation. J Alloy Compd 830:154734
46. Du XQ, Huang JW, Feng YY, Ding Y (2016) Flower-like 3D CuO microsphere acting as photocatalytic water oxidation catalyst. Chin J Catal 37:123–134
47. Chaudhary M, Singh M, Kumar A, Prachi Gautam YK, Malik AK, Kumar Y, Singh BP (2021) Experimental investigation of Co and Fe-Doped CuO nanostructured electrode material for remarkable electrochemical performance. Ceram Int 47:2094–2106
48. Kumar PS, Selvakumar M, Babu SG, Induja S, Karuthapandian S (2017) CuO/ZnO nanorods: An affordable efficient p-n heterojunction and morphology dependent photocatalytic activity against organic contaminants. J Alloy Compd 701:562–573
49. Suganthi N, Thangavel S, Pushpanathan K (2020) Infra-Red Emission and Electrochemical Properties of CuO/ZnO Nanocubes. J Inorg Organomet Polym 30:5224–5233
50. Olad A, Behboudi S, Entezami AA (2012) Preparation, characterization and photocatalytic activity of TiO_2/polyaniline core-shell nanocomposite. Bull Mater Sci 35:801–809
51. Islam MR, Saiduzzaman M, Nishat SS, Kabir A, Farhad SFU (2021) Synthesis, characterization and visible light-responsive photocatalysis properties of Ce doped CuO nanoparticles: A combined experimental and DFT plus U study. Colloid Surf A-Physicochem Eng Asp 617:126386
52. Liu WL, Zhang YF (2018) Blueshift of absorption edge and photoluminescence in Al doped ZnO thin films. Integr Ferroelectr 188:112–120
53. Zheng HP, Langner KM, Shields GP, Hou J, Kowiel M, Allen FH, Murshudov G, Minor W (2017) Data mining of iron(II) and iron(III) bond-valence parameters, and their relevance for macromolecular crystallography. Acta Crystallogr Sect D-Struct Biol 73:316–325
54. Yang Y, Xu D, Wu Q, Diao P (2016) Cu_2O/CuO Bilayered Composite as a High-Efficiency Photocathode for Photoelectrochemical Hydrogen Evolution Reaction. Sci Rep 6:3515855
55. Sharma S, Khare N (2018) Sensitization of narrow band gap Bi_2S_3 hierarchical nanostructures with polyaniline for its enhanced visible-light photocatalytic performance. Colloid Polym Sci 296:1479–1489
56. Luan J, Shen Y, Wang S, Guo N (2017) Synthesis, Property Characterization and Photocatalytic Activity of the Polyaniline/ $BiYTi_2O_7$ Polymer Composite. Polymers 9:69
57. Palve AM (2021) Ultra-fast photoreduction of toxic Cr(VI) by CdS-rGO synthesized using single source precursor. J Alloy Compd 868:159143
58. Villa K, Galan-Mascaros JR (2021) Nanostructured Photocatalysts for the Production of Methanol from Methane and Water. Chemsuschem 14:2023–2033
59. Li JH, Jiang M, Zhou HJ, Jin P, Cheung KMC, Chu PK, Yeung KWK (2019) Vanadium Dioxide Nanocoating Induces Tumor Cell Death through Mitochondrial Electron Transport Chain Interruption. Glob Chall 3:1800058
60. Gao HJ, Yang H, Wang SF (2018) Hydrothermal synthesis, growth mechanism, optical properties and photocatalytic activity of cubic $SrTiO_3$ particles for the degradation of cationic and anionic dyes. Optik 175:237–249
61. Zhang DY, Lv S, Luo Z A study on the photocatalytic degradation performance of a [KNbO3](0.9)-[BaNi0.5Nb0.5O3-delta](0.1) perovskite. RSC Adv 10:1275–1280